ChemComm

COMMUNICATION

View Article Online
View Journal | View Issue

Cite this: *Chem. Commun.*, 2024, 60, 9773

Received 24th July 2024,
Accepted 8th August 2024

DOI: 10.1039/d4cc03712j

rsc.li/chemcomm

Highly sensitive and selective detection of DCP vapors using pyridine-based fluorescent nanofilms†

Zebiao Qiu, Yue Xiao, Ling Zhang, Yupei Miao, Bei Zhang, Xiaolin Zhu, * Liping Ding, * Haonan Peng * and Yu Fang

A novel fluorescent nanofilm DBAP-ETTA has been developed for diethyl chlorophosphate (DCP) vapor detection with high sensitivity and selectivity. Its smooth, homogeneous structure and large Stokes shift enable significant fluorescence quenching upon DCP exposure. The protonation-based sensing mechanism makes it ideal for real-time, portable DCP vapor sensing.

Sarin is an extremely toxic nerve agent that poses severe threat to human health and public safety.[1] Due to its high toxicity and potential use in chemical warfare, the detection and monitoring of Sarin are of paramount importance.[2] However, handling and testing Sarin directly in laboratory settings are highly hazardous and impractical due to its lethal nature. Alternatively, diethyl chlorophosphate (DCP) with a similar chemical structure to Sarin (Scheme S1, ESI†) is commonly used as a simulant in laboratory experiments for developing and validating detection methods.[3] DCP is significantly less toxic, allowing for safer handling and experimentation while still providing relevant insights into the detection mechanisms applicable to Sarin.[4]

Detecting nerve agents, however, presents several challenges. Traditional detection methods, such as chromatography,[5] electrochemical spectroscopy,[6] and mass spectrometry,[7] while effective, have drawbacks including high cost, lengthy analysis time, and the requirement for sophisticated equipment and trained personnel. In contrast, film-based fluorescence sensing techniques have attracted much attention because of their high sensitivity, rapid response, and relatively simple operation.[8] The fluorescent film is the core component of a film-based fluorescence sensing unit, which determines the sensor's detection object and sensing performance.[9] Although many fluorescent sensors for DCP have been developed,[10] they suffer from several limitations. Traditional film preparation methods, such as drop coating,[11] dip coating,[12] spin coating,[13] chemical vapor deposition,[14] *etc.*, are afflicted with issues like the coffee-ring effect, manufacturing complexity, and suboptimal utilization of sensor cells. Additionally, some fluorescent probes have sensitivities at the parts-per-billion (ppb) level, which is not considered optimal.[15] Therefore, innovation in nanofilm preparation methods and rational film structure design is crucial for enhancing fluorescence sensing performance.

To address the aforementioned issues, we employ a film fabrication method based on the Schiff base reaction at the air–liquid interface, rather than a simple physical approach.[16] In this work, we select tetrakis(4-aminophenyl)-ethene (ETTA) as the precursor because TPE is a very famous aggregation-induced emission unit,[17] which guarantees good luminescence properties of solid-state nanofilms. The nonplanar structure of TPE enhances the porosity of the nanofilms at the molecular level, facilitating increased contact between the fluorescent unit and DCP molecules.[18] Furthermore, nitrogen-containing materials, such as pyridine groups, are frequently utilized to construct fluorescent probes for the specific recognition of DCP due to their Lewis basicity.[19] Consequently, we incorporate the pyridine derivative 4,4′-(2,5-pyridinediyl)bis-benzaldehyde (DBAP) as the recognition unit to enhance the film's capability for specific capture and selection of DCP molecules, thereby improving the sensitivity of the film for DCP detection.

In this study, we rationally designed and successfully prepared a novel nanofilm, DBAP-ETTA, as shown in Scheme 1 (see the ESI† for detailed steps). This film boasts a smooth and homogeneous surface, controllable thickness, and substrate adaptability. As anticipated, the film demonstrated rapid and specific recognition, as well as a highly sensitive response to DCP molecules. Notably, it produced a significant response to DCP vapors at a concentration of 0.1 ppt. This advancement not only enhances the overall performance of fluorescence-based sensing systems, but also provides a robust platform for the detection of nerve agent mimics.

As shown in Fig. 1a, the Fourier-transform infrared (FTIR) spectra of the nanofilms lack peaks at 3352 cm^{-1} and 2749 cm^{-1},

Key Laboratory of Applied Surface and Colloid Chemistry (Ministry of Education), School of Chemistry and Chemical Engineering, Shaanxi Normal University, Xi'an 710062, P. R. China. E-mail: phn@snnu.edu.cn, xiaolinchem@snnu.edu.cn, dinglp33@snnu.edu.cn

† Electronic supplementary information (ESI) available. See DOI: https://doi.org/10.1039/d4cc03712j

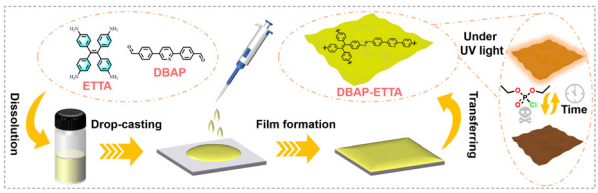

Scheme 1 Schematic representation of the nanofilm preparation process, including the preparation of the precursor solution, drop coating, reaction, and film transferring. Detailed steps are provided in the ESI.†

which correspond to the $-NH_2$ and –CHO functional groups in ETTA and DBAP, respectively. The absence of these peaks indicates that the functional groups in the monomers have reacted, resulting in their near-complete disappearance in the nanofilms. Furthermore, we characterized the absorption spectra of DBAP, ETTA, and DBAP-ETTA (Fig. S1, ESI†). The DBAP-ETTA nanofilm exhibits distinct absorption peaks around 335 nm and 410 nm, which are different from the individual absorption peaks of DBAP (327 nm) and ETTA (285 nm and 357 nm). These variations in the FTIR spectra and absorption spectra confirm the formation of new chemical structures, indicating that the film formation involves chemical interactions rather than simple physical stacking.

Moreover, we conducted X-ray photoelectron spectroscopy (XPS) analysis. The C 1s and N 1s spectra of the nanofilms (Fig. S2, ESI†) exhibit distinct peak shifts that confirm the formation of –C=N– bonds, resulting from the reaction between –C=O and $-NH_2$ groups. These XPS results corroborate the findings from FTIR, providing a comprehensive understanding of the chemical processes involved in the formation of the nanofilms.

As shown in Fig. 1b, the nanofilm exhibits a smooth, homogeneous, and intact surface. Microscopic analyses using scanning electron microscopy (SEM), transmission electron microscopy (TEM), and atomic force microscopy (AFM) also confirm that the nanofilm has a uniform, smooth, and defect-free surface (Fig. 1b–f). The folds observed on the surface of the film under SEM (Fig. S3, ESI†) indicate good flexibility. AFM measurements determine the film thickness to be 73 nm (Fig. 1f). Additionally, by varying the concentration of the precursor solution, the film thickness can be adjusted within the range of 52 to 200 nm (Fig. S4, ESI†), demonstrating that the film thickness can be effectively controlled through the precursor solution concentration. X-ray diffraction (XRD) results (Fig. S5, ESI†) reveal that the nanofilms are amorphous, which is corroborated by the selected area electron diffraction (SAED) (inset of Fig. 1d). Energy-dispersive X-ray (EDX) element mapping (Fig. S6, ESI†) confirms that the nanofilms are primarily composed of carbon (C) and nitrogen (N), with these elements uniformly distributed across the nanofilm's surface.

Under daylight, it appears yellow, while under 365 nm UV light, it emits a bright orange-red fluorescence (Fig. 1h). The ability to load the nanofilm onto an iron ring demonstrates its toughness and self-supporting capability (inset on the left of Fig. 1b). The water contact angle measurement shows an angle of 81° (inset on the right of Fig. 1b), indicating slight

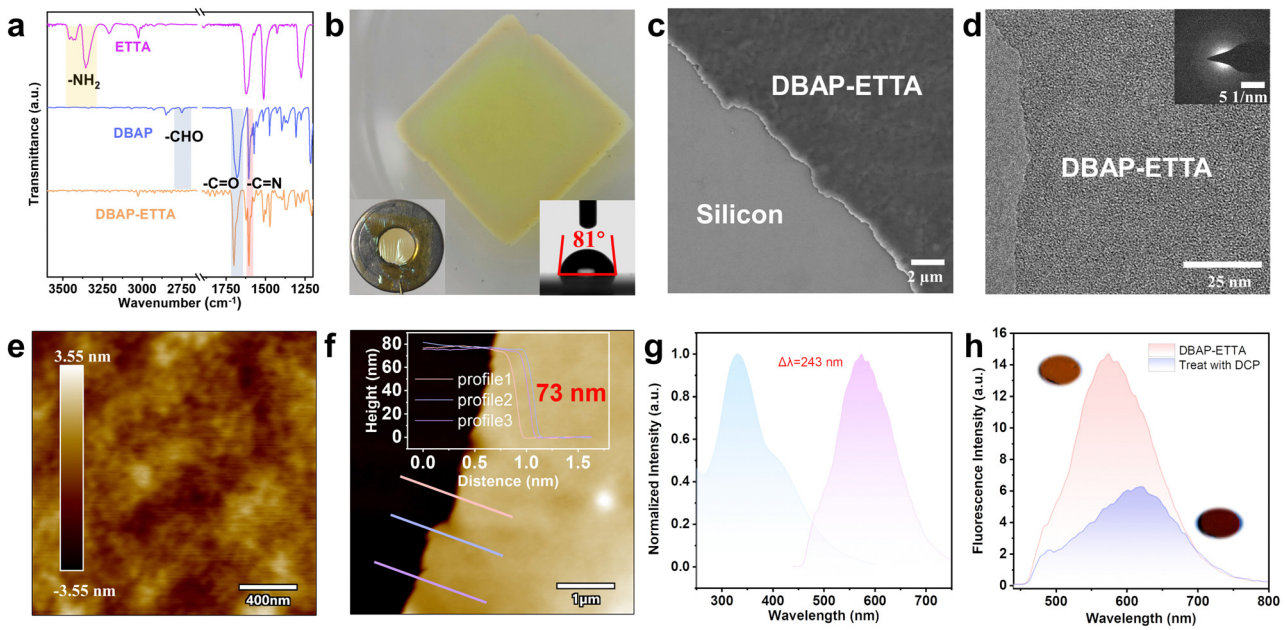

Fig. 1 (a) FT-IR spectra of compounds DBAP, ETTA, DBAP-ETTA. (b) Photographs of the nanofilm DBAP-ETTA, the inset on the left shows the nanofilm loaded on an iron ring, the inset on the right shows the water contact angle results for nanofilm of 81°. (c) SEM image of DBAP-ETTA. (d) TEM image of DBAP-ETTA, inset shows SAED results. (e) AFM images of the nanofilm with a concentration of 0.5%. (f) Cross-section and height distribution of the nanofilm with a concentration of 0.5%. (g) UV absorption and fluorescence spectra of the nanofilm DBAP-ETTA (note: λ_{Ex} = 331 nm, λ_{Em} = 574 nm). (h) Fluorescence emission spectra of the nanofilm before and after DCP treatment (note: the left and right insets in graph (b) show pictures of nanofilm DBAP-ETTA under 365 nm UV light before and after exposure to DCP vapor, respectively).

hydrophilicity. These findings collectively demonstrate the films' structural integrity, flexibility, and tunable thickness, highlighting their potential for various applications.

The fluorescence emission and absorption spectra of the nanofilm were measured, which exhibits an absorption maximum at 331 nm and an emission maximum at 574 nm, resulting in a large Stokes shift of 243 nm (Fig. 1g). This substantial Stokes shift helps to reduce the sensor device's signal-to-noise ratio, thereby enhancing its sensitivity. Upon exposure to DCP vapor fumigation, the nanofilms exhibited significant fluorescence quenching, achieving a quenching efficiency of 75% (Fig. 1h). This pronounced sensing response underscores the nanofilm's potential for effectively detecting DCP vapors.

To further investigate the sensing behavior of the nanofilms towards DCP vapors, a dedicated sensing test platform was constructed in the laboratory. As illustrated in Fig. 2a, the platform comprises a sample feeding system, a sensing unit, and a data conversion and transmission system. The prepared sensing nanofilm was mounted on the surface of a quartz wafer, which was then placed inside the sensor. The test gas was precisely controlled to enter the sensor through a control panel (Fig. 2b), inducing a change in the fluorescence intensity of the nanofilm. This change in the optical signal was subsequently converted into an electrical signal by the data conversion and transmission system, which then relayed the data to a computer for analysis.

The nanofilms were irradiated on the sensing platform using a 331 nm wavelength light source. As shown in Fig. 3a, the fluorescence intensity of the film decreased by only 11% over 7 hours, demonstrating good photostability. Additionally, to evaluate the selectivity of the nanofilms, responses to 17 common volatile organic and inorganic reagents were measured (Fig. 3b).[20] Among these, DCP vapor triggered a significant fluorescence quenching response. Interestingly, the sensor's response to HCl and DCP differs significantly. This

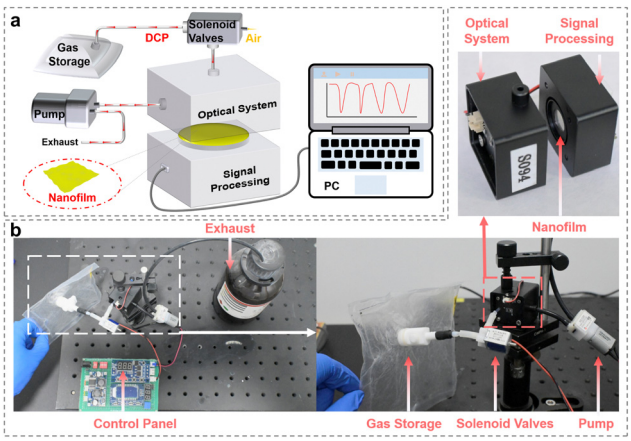

Fig. 2 (a) Schematic diagram of the sensing system, (gas storage, solenoid valves, and pumps): exhaust treatment to form the sample feeding system, nanofilm acts as the core sensing unit, and sensors and computers form the data conversion and transmission systems. (b) Photographs of sensing test systems.

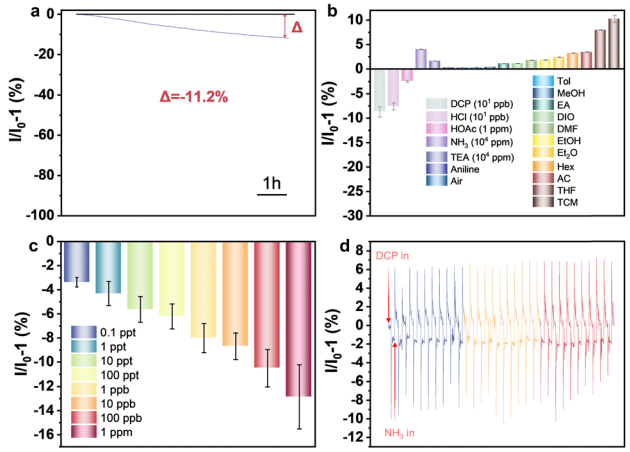

Fig. 3 (a) Photostability testing of DBAP-ETTA. (b) Selectivity testing of DBAP-ETTA for DCP vapors containing 17 interferents was performed. (c) Sensitivity test result of DBAP-ETTA for DCP detection. (d) Reproducibility of DBAP-ETTA for DCP detection (note: the error bars in the graph b and c mean values are standard deviation of three independent experiments).

distinction is evident from the response kinetic curves (Fig. S7a, ESI†), which show that the response curves for HCl and DCP are distinctly different. The specific interaction between DCP and the nanofilm leads to a unique response pattern, underscoring the sensor's specificity for DCP.

Furthermore, the sensitivity of the nanofilms was tested with varying concentrations of DCP vapor from 0.1 ppt to 1 ppm (Fig. 3c). The nanofilms exhibited a significant response to DCP vapor at concentrations as low as 0.1 ppt, highlighting their superior detection capability. The recovery of the film was achieved by alternating exposure to DCP vapor, air, and NH_3 vapor (Fig. S7b, ESI†). Under these conditions, the nanofilms maintained consistent performance over at least 30 cycles (Fig. 3d), demonstrating their robustness and reliability.

To further investigate the response mechanism of the nanofilms to DCP vapor, IR and XPS spectra of the films before and after DCP treatment were measured. As shown in Fig. 4a, the IR spectra of the nanofilms after DCP treatment exhibited a distinct new peak at 1645 cm^{-1}, attributed to the formation of a C=N–H^+ bond,[21a] which can be attributed to the

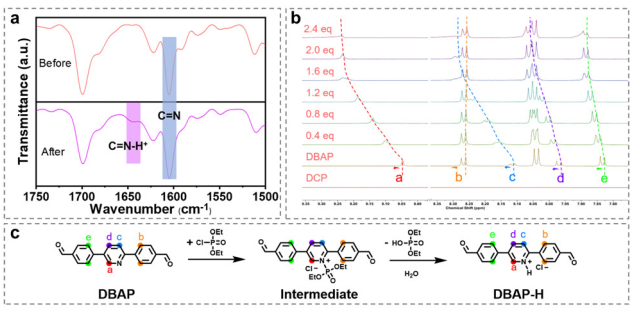

Fig. 4 (a) FT-IR spectra of the DBAP-ETTA before and after DCP treatment. (b) ^{1}H NMR spectra of the compound DBAP with different equivalence ratios of DCP addition. (c) Proposed mechanism of binding of the compound DBAP to DCP.

protonation of the nitrogen atoms in the pyridine ring and the imine bond,[4a] facilitated by the acidic environment created by the hydrolysis of DCP. This observation is further confirmed by the XPS results (Fig. S9, ESI†).

Additionally, NMR titrations of DBAP, the building block of the films, were conducted with the addition of different equivalents of DCP (Fig. 4b). The results indicated that the N atom in the pyridine moiety is protonated upon the addition of DCP. This occurs because, during DCP hydrolysis, acidic by-products such as HCl are formed, which can protonate the nucleophilic pyridinyl nitrogen atom. The phosphorus atom in DCP is attacked by the nucleophilic pyridinyl nitrogen atom, resulting in an intermediate that loses its diethyl phosphate group and becomes the final protonated product, DBAP-H (Fig. 4c). This protonation was also confirmed by high-resolution mass spectrometry (Fig. S11, ESI†). This process leads to intramolecular charge rearrangement. Specifically, the chemical shifts of H_a, H_c, H_d, and H_e moved downfield, while Hb exhibited a slight upfield shift. These shifts indicate that DBAP binds effectively and specifically to DCP.[21b] To further demonstrate the critical role of the pyridine unit in the sensing process, we prepared the control nanofilm TPDA-ETTA with a benzene ring structure instead of a pyridine structure (Fig. S12a and b, ESI†). And the sensing results showed that it could produce only 0.3% response intensity to 1 ppm concentration of DCP vapor (Fig. S12c, ESI†), which is far inferior to that of DBAP-ETTA.

In summary, we successfully developed a novel fluorescent nanofilm DBAP-ETTA for high sensitivity and selectivity DCP detection. The nanofilm exhibits homogeneity, flexibility, and controllable thickness. Its large Stokes shift enhances fluorescence detection. The nanofilm selectively detects DCP vapors and maintains its performance through multiple NH_3 vapor fumigation cycles. It shows transient and extremely sensitive responses to DCP vapor, with a significant response at 0.1 ppt, attributed to its high porosity and strategic incorporation of pyridine moieties. These findings highlight the potential of combining pyridine derivatives with highly porous nanofilms for detecting the nerve agent simulant DCP.

This work was supported by the National Key Research and Development Program of China (2022YFA12055002), the National Natural Science Foundation of China (22272101, 22202128), the Program of Introducing Talents of Discipline to Universities (111 project, B14041), the Shaanxi Fundamental Science Research Project for Chemistry and Biology (23JHQ 074), the Scientific Research Plan of Shaanxi Province of China (2021TD-18), and the Fundamental Research Funds for the Central Universities (GK202305001).

Data availability

The data supporting this article have been included as part of the ESI.†

Conflicts of interest

There are no conflicts to declare.

Notes and references

1 (*a*) C. R. Jabbour, *et al.*, *Nat. Rev. Chem.*, 2021, **5**, 370–387; (*b*) Z. Zhou, *et al.*, *Aggregate*, 2024, e629; (*c*) M. Yao, *et al.*, *Adv. Fiber Mater.*, 2023, **5**, 1632–1642.
2 (*a*) W. Mo, *et al.*, *Nat. Commun.*, 2022, **13**, 5189; (*b*) B. T. Zhu, *et al.*, *Coord. Chem. Rev.*, 2022, **463**, 214527; (*c*) V. Kumar, *et al.*, *Chem. Soc. Rev.*, 2023, **52**, 663–704.
3 (*a*) P. Zheng, *et al.*, *Sens. Actuators, B*, 2020, **322**, 128611; (*b*) S. Zhang, *et al.*, *ACS Sens.*, 2023, **8**, 1220–1229; (*c*) P. Zheng, *et al.*, *J. Hazard. Mater.*, 2021, **415**, 125619.
4 (*a*) T. Sultana, *et al.*, *Anal. Methods*, 2024, **16**, 759–771; (*b*) W. Xu, *et al.*, *ACS Sens.*, 2016, **1**, 1054–1059.
5 P. Sarkar, *et al.*, *J. Mol. Struct.*, 2024, **1306**, 137846.
6 R. Kaur, *et al.*, *ACS Appl. Nano Mater.*, 2024, **7**, 12605–12619.
7 (*a*) Z. Abbas, *et al.*, *J. Mater. Chem. C*, 2021, **9**, 10037–10051; (*b*) E. D. Fussell, *et al.*, *ACS Sens.*, 2024, **9**, 2325–2333.
8 (*a*) R. Huang, *et al.*, *Chem. Soc. Rev.*, 2024, **53**, 6960–6991; (*b*) H. Peng, *et al.*, *J. Phys. Chem. Lett.*, 2024, **15**, 849–862; (*c*) K. Liu, *et al.*, *J. Am. Chem. Soc.*, 2023, **145**, 7408–7415; (*d*) D. Zhao, *et al.*, *Chem. Commun.*, 2022, **58**, 747–770.
9 (*a*) X.-Y. Zhang, *et al.*, *Coord. Chem. Rev.*, 2020, 417; (*b*) S. Xing and C. Janiak, *Chem. Commun.*, 2020, **56**, 12290–12306.
10 (*a*) Q. Chen, *et al.*, *Anal. Chem.*, 2023, **95**, 4390–4394; (*b*) Y. Lei, *et al.*, *Sens. Actuators, B*, 2023, 396; (*c*) F. Xiao, *et al.*, *Angew. Chem., Int. Ed.*, 2024, **63**, e202400453.
11 Y. Yao, *et al.*, *Sens. Actuators, B*, 2022, **352**, 131044.
12 T. Han, *et al.*, *Sci. Total Environ*, 2020, **746**, 141412.
13 (*a*) A. H. Ashoka and A. S. Klymchenko, *ACS Appl. Mater. Interfaces*, 2021, **13**, 28889–28898; (*b*) X. Li, *et al.*, *eScience*, 2023, **3**, 100084.
14 J. Chen and W. Xu, *eScience*, 2023, **3**, 100178.
15 (*a*) C. Chen, *et al.*, *Anal. Methods*, 2024, **16**, 515–523; (*b*) J. Chourasia, *et al.*, *Luminescence*, 2024, **39**, e4731.
16 M. Li, *et al.*, *Anal. Chem.*, 2023, **95**, 2094–2101.
17 (*a*) Z. H. Zhu, *et al.*, *Adv. Funct. Mater.*, 2021, **31**, 2106925; (*b*) M. Yang, *et al.*, *Chem. Soc. Rev.*, 2022, **51**, 8815–8831; (*c*) X. Feng, *et al.*, *Chem. Soc. Rev.*, 2023, **52**, 6715–6753.
18 (*a*) Q. Wang, *et al.*, *Chin. J. Chem.*, 2022, **40**, 1359–1385; (*b*) X. Liu, *et al.*, *Sci. Adv.*, 2024, **11**, 2400101.
19 (*a*) X. Huang, *et al.*, *ACS Mater. Lett.*, 2021, **3**, 249–254; (*b*) Y. M. Zhang, *et al.*, *Sens. Actuators, B*, 2021, **343**, 130140; (*c*) C. Chen, *et al.*, *Anal. Methods*, 2024, **16**, 515–523.
20 Usually, highly volatile compounds were considered as analytes, rather than low-volatility compounds, such as phosphate derivatives, *etc.* (*a*) Y. J. Jang, *et al.*, *New J. Chem.*, 2017, **41**, 1653–1658; (*b*) A. Maji, *et al.*, *Anal. Methods*, 2023, **15**, 6417–6424.
21 (*a*) X. Zhu, *et al.*, *Angew. Chem., Int. Ed.*, 2024, **63**, e202405962; (*b*) X. Zhu, *et al.*, *J. Mater. Chem. C*, 2023, **11**, 11671–11680.

